

Perforation of aluminum plates by fragment simulating projectiles (FSP)

T. Fras*¹, **L. Colard**¹ and **P. Pawlowski**²

¹French-German Research Institute of Saint-Louis (ISL),
Saint-Louis, France

²Institute of Fundamental Technological Research, Warsaw, Poland

ABSTRACT

The paper describes the ballistic impact test, in which fragment simulating projectiles (FSPs) of a 20-mm-diameter have been used against 40-mm-thick plates made of an aluminum alloy AA7020-T651. To perforate plates, the projectiles must have reached a velocity higher than 890 m/s. Based on the performed ballistic test, the plugging failure mode is numerically modeled using the LS-DYNA software package. Results obtained due to the calculations in the Finite Element Method (FEM) are compared with the results from the Smoothed Particle Hydrodynamics (SPH). A condition of geometrical similarity between the target deformed experimentally and its numerical representation is introduced to evaluate the performed simulations.

Keywords: Ballistic impact test, Fragment simulating projectile (FSP), Plugging failure mode, Smooth Particle Hydrodynamics (SPH), Optical scanning

1. INTRODUCTION

Generally, projectiles can be grouped depending on their nose shapes, i.e. blunt-, ogive- (conical) or round- (hemispherical) nosed projectiles, [1]. Fragment Simulating Projectiles (FSPs) are standard military penetrators of a non-axisymmetric geometry used to simulate artillery shell fragments, [2]. Since this kind of projectiles is used mainly to evaluate a protection level in the component acceptance tests, [3–4], reports describing FSP influences on a structure are relatively rare. The analysis presented here is complementary to studies analyzing target response to impacts of the projectiles of other shapes, [5–10]. The target material is an aluminum alloy AA7020-T651 (Aluminum-Zinc Wrought Alloy, AlZn4.5Mg1, 3.4335) which physical and mechanical properties, as well as a good weight-strength ratio results in its frequent applications to light armored protection structures, [11]. In order to verify ballistic performance of the discussed alloy, the ballistic impact tests are performed and analyzed.

Due to numerical simulations, a material response to impacts is easier to understand on condition that the simulation is carefully and accurately prepared and a chosen material model is based on the proper material characterization. In the discussed case, the aluminum alloy is modeled by the coupled Johnson-Cook model, [12–13]. The JC model [12] may be used to describe a material stress-strain response to large strains and temperatures. The Johnson-Cook fracture model [13] allows for calculations of the damage accumulation in the

*Corresponding Author: E-mail: teresa.fras@isl.eu

material, due to which the material failure is estimated. For AA7020-T651, the parameters of the model have been determined basing on the series of compression tests at different strain rates and temperatures. The JC model is implemented in LS-DYNA code and may be applied in calculations performed using the Finite Element Method (FEM) and the Smooth Particle Hydrodynamics (SPH).

The main advantages of the Lagrangian finite elements formulation [14] is an intuitive modeling of an experimental configuration by a deformable geometry, a large number of implemented material models, as well as many examples describing successful applications, [7–10]. The main criticism of the Lagrangian FEM is a large mesh distortion, [15–16], since the heavily deformed elements may cause numerical difficulties leading to the negative volume of elements. In order to eliminate distorted elements, the erosion threshold condition is used (there are other – however, not so popular - possibilities, like a ‘pilot hole’, [16]). The material erosion is a purely numerical technique due to which distorted elements are removed from the mesh according to a certain erosion criterion, which defines a predetermined value of deformation. As there are several criteria which determine element erosion, the method has opponents who disapprove its arbitrariness.

SPH (Smoothed Particle Hydrodynamics) is a meshless Lagrangian method used mainly to model problems occurring under high velocity impacts. The material geometry is discretized by a number of nodes, representing particles to which material characteristics are assigned. In comparison to FEM, the major advantage of SPH is a material deformation without severe mesh distortion – no algorithm of element erosion is required. The fundamentals of SPH theory can be found in [15, 17]. Initially, SPH was aimed for astrophysical problems [18–19]. Nowadays, it is widely applied in mechanics and dynamics of metals and fluids, and considered as comparative to the classical FEM, [15, 20]. In several papers, e.g. [21–23], it is presented that the SPH method may be used successfully to model response of structures under high velocity impact loads. On the other hand, some authors encounter for problems of improper material failure modeling, [16]. In [22], it is also noticed that the SPH method may be less efficient computationally compared to FEM and that it suffers from certain instability problems, [21].

The paper addresses the question which of the above-mentioned numerical techniques allows for an optimal simulation of the FSPs impacts into the aluminum plates. The observed material response to the impacts is analyzed in order to understand phenomena responsible for the material failure. The target-projectile interaction is modeled numerically, which allows the observations and conclusions to be verified. As one of criteria due to which the numerical simulation is evaluated, the geometrical similarity between the experimental plug and its numerical representation is used.

2. BALLISTIC PERFORMANCE OF AA7020-T651 UNDER FSP IMPACTS

The aluminum alloy AA7020-T651 belongs to a group of Aluminum Zinc Magnesium (AlZn4.5Mg1,3.4335) wrought ternary alloys, which advantages are a lack of corrosion and a good strength - weight ratio. The material may be subjected to extremes of environmental exposures, including both low and high temperatures, high pressures and highly corrosive and reactive fluids, [26–27]. Consequently, AA7020-T651 is widely used in welded engineering structural components, military and aerospace applications. The chemical composition of AA7020-T651, defined in European Standards EN 573-1 and 573-2, is given in Table 1. The investigated aluminum alloy was delivered as rolled plates, tempered and aged in T651 conditions (defined in Standard EN 515).

Table 1: Chemical composition of AA7020-T651 (wt %)

| | Zn | Mg | Cu | Si | Fe | Mn | Ti+Zr | Cr | Zr |
|--------|-----|------|-------|------|------|------|-------|------|------|
| AA7020 | 4-5 | 1.13 | 0.002 | 0.13 | 0.23 | 0.32 | 0.128 | 0.12 | 0.11 |

The target plates were manufactured as cylinders of 120 mm diameter and 40 mm thickness. The cylindrical samples were tightly pressed inside the aluminum frame (made of the commercial alloy AA6061-T651) which stabilized samples for shots, Figure 1(a). The configuration presented in Figure 1(a) allows samples of reduced size to be tested.

Dimensions and material properties of the impactors – Fragment Simulating Projectiles (FSPs) - fulfill the requirements of Military Specification MIL-P-46593A, [2]. 20 mm FSPs weighting 53.8 grams simulates a 155 mm artillery shell fragment in procedures of evaluating a protection level of logistic and light armored vehicles, [2–3]. It has a flat nose and a non-axisymmetric shape – as it is shown in Figure 1(b), [3]. The FSP consists of an AISI 4340-H steel alloy, heat-treated to a hardness of HRC 30 ± 1. Some physical properties of the target and projectile materials are compared in Table 2.

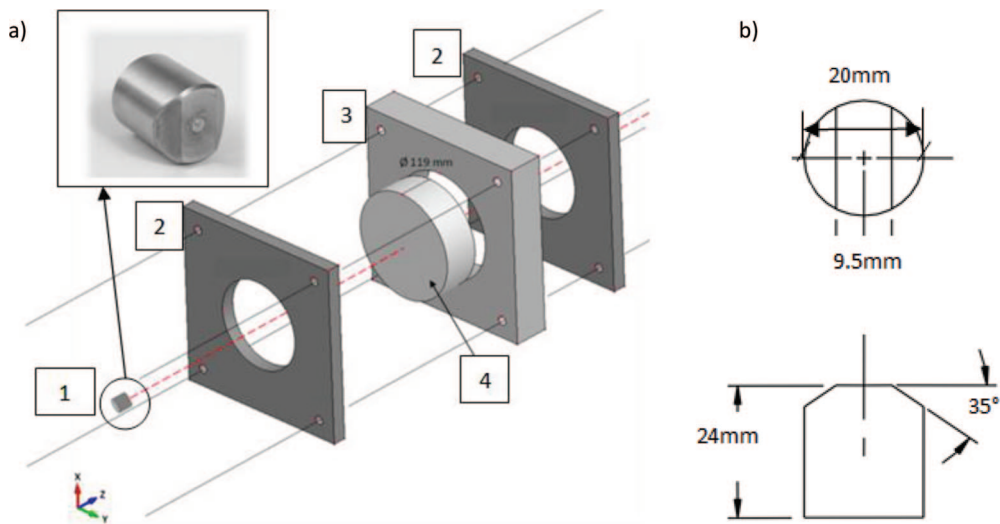


Figure 1: (a) Experimental configuration for impact tests: 1) projectile, 2) steel frames, 3) aluminum frame, 4) target. (b) Geometry of a 20 mm FSP

Table 2: Physical properties of AA7020-T651 and Steel 4340-H

| | Steel 4340-H | AA7020-T651 |
|-----------------------------|------------------------|-------------|
| ρ [kg/m ³] | 7850 | 2770 |
| G [GPa] | 80 | 25 |
| E [GPa] | 205 | 71 |
| ν [-] | 0.3 | 0.3 |
| C _p [J/kg.K] | 475 | 910 |
| Hardness | 30 HRC ± 1 (300 HV) | 133 HV ± 2 |

A ballistic limit curve for the 40 mm thick AA7020-T651 plates was determined basing on the shots of 20 mm FSPs, Figure 2(a). The curve is given as a dependence between the initial (v_0) and residual (v_R) projectile velocities. In the discussed case, the ballistic limit velocity, i.e. the greatest impact velocity which the target can withstand without being perforated, is close to $v_{bl.exp} \approx 900$ m/s. The experimental data are fitted to a model proposed by Lambert (1978) [24], in which the residual projectile velocity (v_R) of a long eroding rod is calculated as a function of the measured initial projectile velocity (v_0) and the experimentally obtained ballistic limit velocity, $v_{bl.exp}$. Due to a curve fitting by the method of least squares with the assumption that the ballistic limit velocity is taken directly from the experimental data, the model constants, a and p , are estimated as $a = 0.85$ and $p = 1.23$.

During the penetration, the deformation mode of a target changes from a ductile hole enlargement, through a mechanism of highly localized shear around the projectile nose, to a combination of plugging and discing (scabbing) mode, Figure 2(b–c). Such failure modes are characteristic for a ductile, anisotropic material, when the texture influences a fracture direction, [25].

The discing leads to a material separation within same planes, parts of such planes are thrown away from a target, Figure 2(c). This failure mode is observed for impact velocities higher than 1200 m/s. According to [25], this kind of fracture is caused by a shear mechanism as it takes place along planes which are intersected by bands of intense shearing. A remained plate thickness, below the projectile, is stretched and bended forward. Bending takes place more easily because it is presented over series of thin layers (resulted from the subsequent processes of rolling during the material manufacturing) rested at the rear side of a target plate.

The plugging failure of target plates is observed for the shots of impact velocities lower than 1200 m/s, Figure 2(b). A plug is a part of a metallic material which is sheared out from a target plate by a deformed projectile, Figure 3. In the initial stage of the deformation, the

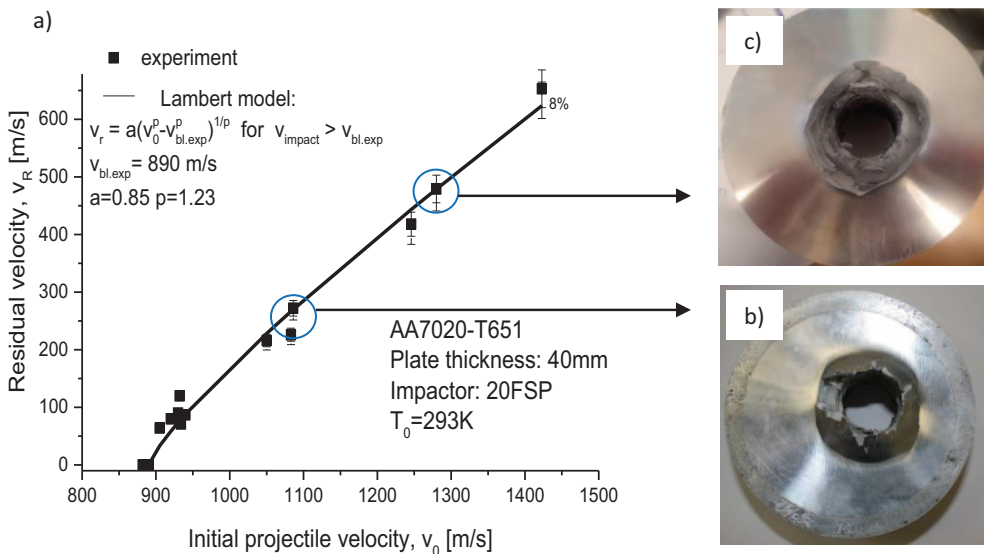


Figure 2: (a) Ballistic curve for 40 mm thick plates made of AA7020-T651 impacted by 20 mm FSPs at ambient temperature. (b) Plates deformed due to the FSP impacts with initial velocities close to 1100 m/s and (c) 1300 m/s

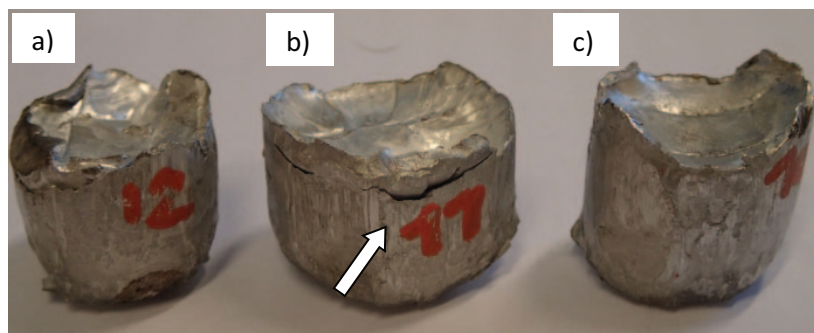


Figure 3: Plugs resulting from impacts with initial velocities close to (a) 900 m/s, (b) 950 m/s and (c) 920 m/s

target material is pushed aside and compressed in front of the projectile - causing an enlargement of the penetration channel. The target material moves ahead of the projectile leading to the bulge formation on the rear plate surface. The large shear strains develop in the target at the periphery of the projectile, highly localized shear bands occur and the process changes to a plug formation, which final step is the plug ejection.

The mass of plugs differs depending on the impact velocity of the projectile. The average height of plugs is about 23 mm but an area of its intersection increases with increasing velocities. The resulted plug mass varies from 31 g ($v_0 = 900$ m/s) to 41 g ($v_0 = 950$ m/s). No projectile parts remain on the plug after the impact – the steel of which projectiles are made is characterized by hardness much greater than hardness of aluminum, Table 2. The plugs remaining after the impacts with initial velocities close to 900 m/s are presented in Figure 3. A horizontal crack in the plug is observed in Figure 3(b), similar cracks occur inside the penetration channel. These cracks are a kind of ‘delamination’ between the internal material layers resulting from the manufacturing processes, i.e. rolling.

The shear zones occur in a material when the rate of work softening due to the heat generated in plastic flow is greater than the rate of work hardening, [25]. A failure mode of targets is determined by the material hardness and a ratio of the plate thickness to the penetrator size (the larger the area of impact zone, the greater the tendency towards penetration by the plugging mechanism, [5]). According to [5], a relatively little material deformation and no lateral compression occurs during the plugging of a blunt nosed projectile in comparison to ‘pushing-aside’ mechanisms, when the penetrator forces its way through an armor by displacing the material sideways. Also, less energy is absorbed during plugging than in cases when the perforation is caused by sharp-nosed projectiles.

3. MATERIAL MODELING

In order to understand mechanisms occurring in a material subjected to the impact, it is necessary to know its mechanical properties and conditions leading to its failure. A thermo-viscoplastic constitutive model and a fracture criterion are determined for AA7020-T651 basing on the quasi-static and dynamic compression tests results at different temperatures. The Johnson-Cook model coupled with the fracture criterion, [12–13], is hereby proposed since it accounts for the effects of strain rate and temperature, as well as it describes the damage accumulation. The simplicity of the JC model calibration combined with a large number of examples presenting satisfying results of ballistic impact modeling (e.g. [5–10]), as well as its implementation in commercial codes speak in favor of this approach. The JC

model includes the effects of the strain path, strain rate, temperature and the stress triaxiality in the flow stress, Eqn (1). The equivalent stress depending on the strain, strain rate and temperature is defined as a function:

$$\sigma(\varepsilon, \dot{\varepsilon}, T) = [A + B\varepsilon^n] \left[1 + C \ln \frac{\dot{\varepsilon}}{\dot{\varepsilon}_{ref}} \right] \left[1 - \left(\frac{T - T_0}{T_m - T_0} \right)^m \right] \quad (1)$$

where A, B, C, m, n are material constants and T_0 , T_m – reference and melting temperature.

In Figure 4(a), the effect of the strain rate for AA7020-T651 is shown as the dependence between the yield strengths, determined for an offset strain equal to 0.1, and the strain rate given in a logarithmic scale. The discussed alloy is not very sensitive to the rate of compressive loading. Low strain rates have a minor influence on the flow stress and the stress is a linear function of strain rates. The AA7020-T651 displays sensitivity to temperature; data are collected in Figure 4(b). Increasing temperature leads to a decrease of yield stress values. This effect is stronger at higher temperatures.

A set of parameters of Eqn (1) is entirely based on the results of the compression tests carried out in the normal direction (which is also the impact direction). The hardening parameters A, B, C, n and m are determined basing on the compression tests performed at different strain rates and temperatures, Table 3.

Since the damage evolution is related to irreversible strains, it may be taken as a function of the accumulated plastic strain. Consequently, the degradation of a material and its damage contribute to the localization of plastic deformation in the penetration process. Fracture occurs when the damage parameter D reaches the value of 1. The damage accumulation is expressed by Eqn (2).

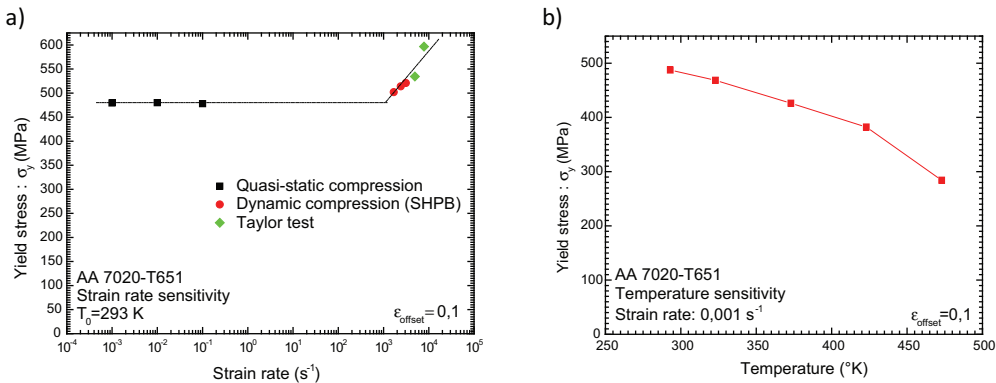


Figure 4: (a) Strain rate sensitivity and (b) temperature sensitivity of AA7020-T651

Table 3: The parameters of JC model for AA7020-T651 obtained due to the own experimental results

| | A (MPa) | B (MPa) | n | C | m | T_m (K) | Reference strain rate (s^{-1}) |
|-------------|------------|------------|------|---------|------|-----------|--|
| AA7020-T651 | 295 | 260 | 1.65 | 0.00089 | 1.26 | 880 | 0.0001 |

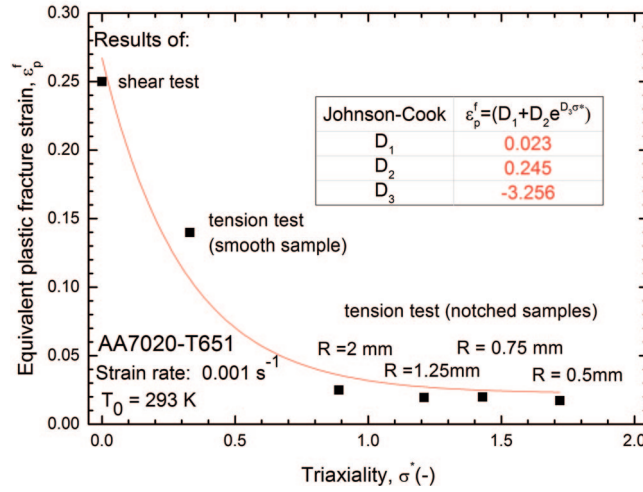


Figure 5: Average fracture strain against the stress triaxiality for the quasi-static tensile tests at room temperature

$$D = \sum \frac{\Delta \epsilon}{\epsilon_f} \tag{2}$$

where $\Delta \epsilon$ is the incremental effective plastic strain and ϵ_f is the equivalent plastic fracture strain.

Johnson and Cook [13] proposed also a function describing the fracture strain depending on the stress triaxiality, strain rate and temperature. The function is given in Eqn (3).

$$\epsilon_f(\sigma^*, \dot{\epsilon}, T) = [D_1 + D_2 e^{D_3 \sigma^*}] [1 + D_4 \ln \dot{\epsilon}] \left[1 + D_5 \frac{T - T_0}{T_m - T_0} \right] \tag{3}$$

where $D_1 - D_5$ are fracture model constants, σ^* is the stress triaxiality ratio.

The parameters of the function which describes the fracture strain, Eqn (3), are obtained experimentally ($D_1 = 0.023$, $D_2 = 0.24$ and $D_3 = -3.26$) and the parameters $D_4 - D_5$ ($D_4 = 0.15$ and $D_5 = 16.8$) were taken from [28], where the properties of an alloy AA5083-H116 are discussed. Figure 5 presents the average fracture strain as a function of the initial stress triaxiality at room temperature obtained due to the tensile test of notched specimens at room temperature and at quasi-static strain rate.

The Johnson-Cook material model, Eqns (1–3), is implemented in LS-DYNA and may be applied in the classical Finite Element Method as well as in the Smoothed Particle Hydrodynamics, [29]. Both techniques may be used to describe a material behavior under high velocity impacts. In the next paragraph, the failure of aluminum plates perforated by the FSP projectiles with impact velocities lower than 1200 m/s is analyzed by the numerical simulation.

4. NUMERICAL MODELING OF THE FSP IMPACT

Analysis of mechanical and thermal properties of AA7020-T651 provided the parameters of the constitutive relation and fracture criterion, Eqns (1–3). The model parameters are collected in Table 3. The Johnson – Cook constitutive model and the function describing the

fracture strain, Eqns (1–3), are implemented in the code via *MAT_015_JOHNSON_COOK. This material type (several implementations of the Johnson – Cook model are proposed in LS –DYNA) is supposed to be used for calculations in which the strain rates vary over a wide range and accounts for temperature increases. It requires an application of an equation-of-state. In the discussed case, the Grüneisen nonlinear equation of state is used, *EOS_GRUNEISEN, in which pressure is defined as a dependence between the shock velocity u_s and the particle velocity u_p variables, Eqns (4–5).

$$u_s = C_0 + S_1 u_p + S_2 \left(\frac{u_p}{u_s} \right) u_p + S_3 \left(\frac{u_p}{u_s} \right)^2 u_p \quad (4)$$

where S_1 , S_2 , and S_3 are the unitless coefficients of the slope of the $u_s - u_p$ curve, γ_0 is the unitless Grüneisen gamma defined as $\gamma = \frac{\gamma_0 - a\mu}{1 + \mu}$ where a is the unitless, first order

volume correction to γ_0 and $\mu = \frac{1}{V} - 1$ is compression defined in terms of relative volume V .

Consequently, for $\mu > 0$ $P(\mu, E)$ is written as it is shown in Eqn (5).

$$P(\mu, E) = \frac{\rho_0 C_0^2 \mu \left[1 + \left(1 - \frac{\gamma_0}{2} \right) \mu - \frac{a}{2} \mu^2 \right]}{\left[1 - (S_1 - 1) \mu - S_2 \frac{\mu^2}{\mu + 1} - S_3 \frac{\mu^3}{(\mu + 1)^2} \right]} + (\gamma_0 + a\mu) E \quad (5)$$

When $\mu < 0$, then Eqn (5) has the form: $P(\mu, E) = \rho_0 C_0^2 \mu + \gamma_0 E$. Table 4 shows the Grüneisen parameters which are taken from [30] and were obtained for an alloy AA7075-T6.

The material anisotropy and the material texture are not accounted for in the numerical calculations. The constitutive behavior and the fracture process of the material are assumed to be isotropic.

4.1. 3D FEM APPROACH

In the first approach, an explicit solver of the Lagrangian Finite Elements Method is used to model the plugging failure mode. The model geometry is based on the experimental configuration shown in Figure 1(a). It is prepared using 3D solid elements, since FSPs have a non-axisymmetric shape. Due to the symmetries of geometry and load case, only a quarter of the configuration is modeled by application of the 8-node constant-stress solid elements with one integration point and stiffness-based hourglass control. A fine mesh of element size $0.5 \times 0.5 \times 0.5$ mm is assumed in the middle zone of the plate where the direct impact influence is observed. At the edge of the target, a mesh of element size $1 \times 1 \times 0.5$ mm is applied. The projectile is meshed regularly; an element size is $0.3 \times 0.3 \times 0.3$ mm.

Table 4: Parameters of the Grüneisen equation of state, [30]

| | C_0 | S_1 | S_2 | S_3 | γ_0 | a |
|-----------|-------|-------|-------|-------|------------|------|
| AA7075-T6 | 0.52 | 1.36 | 0 | 0 | 2.2 | 0.48 |

The model of the target results in approximately 450 000 elements, the frame is modeled with 2500 elements; the projectile consists of 28000 elements. The proposed mesh is regularized by an application of the card *MAT_NONLOCAL. The values of its parameters are assumed according to data provided by [29, 31]; $p = 8$, $q = 2$.

The boundary conditions of the model are presented in Figure 6. The frame is fully clamped, the plate is in contact with the frame (*AUTOMATIC_SURFACE_TO_SURFACE) and an initial velocity is applied to the projectile. The contact between the target and projectile is modeled using an eroding algorithm (*ERODING_SURFACE_TO_SURFACE), due to which the element erosion is applied to the model. Friction between parts is not considered. The elements are removed from the target material upon reaching a certain value defined by the failure conditions introduced to the calculation by the card *MAT_ADD_EROSION. As it is known that the plugging failure mode results from shearing stresses occurring in a ductile material at the periphery of the projectile, [6, 25], the failure criterion is fulfilled when the shear strain at failure reaches its 100%, i.e. $EPSSH = 1.0$.

The projectile is made of 4340-H steel, for which the material constants of the JC material model are taken from the study of Johnson and Cook [12], Table 5. The projectile deformation is determined by means of the simplified version of the JC model defined in the code by the card *MAT_98_SIMPLIFIED_JOHNSON_COOK. The elements are eroded when the effective plastic strain at failure reaches an assumed value, in this case $p_{fail} = 1.0$.

Basing on the presented geometry and the discussed material model – the target material response to the FSP impacts is calculated. In Figure 7, the numerical and experimental curves presenting dependence between initial and residual velocities are plotted. The calculated value of the ballistic limit is close to the experimental one (i.e. $v_{bl,num} = 870$ m/s

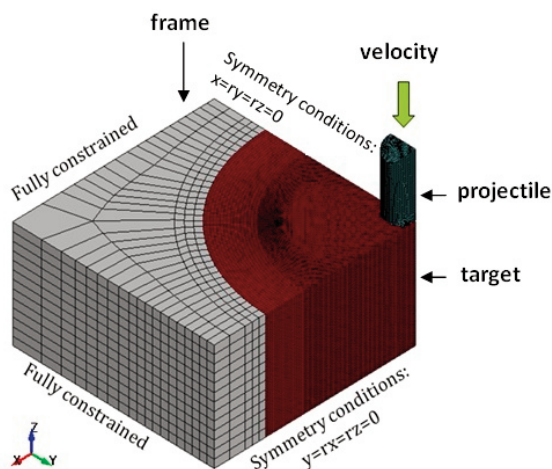


Figure 6: Boundary conditions of the experimental configuration

Table 5: The parameters for the JC model for 4340-H steel

| | A (MPa) | B (MPa) | n | C | m | T _m (K) | Reference strain rate (s ⁻¹) |
|--------------|---------|---------|------|-------|------|--------------------|--|
| Steel 4340-H | 791 | 510 | 0.26 | 0.014 | 1.03 | 1793 | 0.001 |

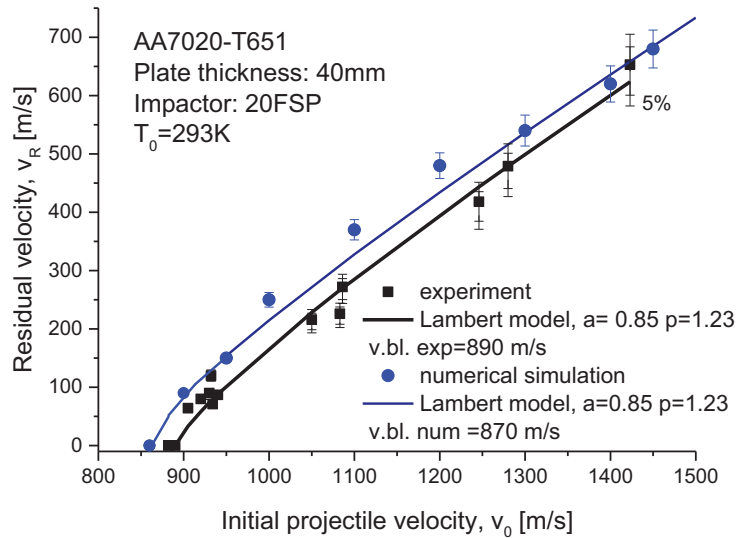


Figure 7: Numerically predicted ballistic curve compared with the experimental one

and $v_{bl,exp} \approx 890$ m/s) but the ballistic curve obtained numerically overestimates values of the experimental residual velocity.

The so called ‘penetration channel’ is a zone where the target deformation is the severest – the target material under the projectile nose is pushed and compressed up to its complete perforation. Outside this zone, almost no material deformation is observed. Between the two parts – the target material inside the penetration channel which is pushed to the rear plate surface and the material outside the channel which does not move – the shearing is observed. It is a dominant failure leading to a localized plugging. Figure 8 shows the maps of shear stresses occurring in a 40 mm thick AA7020-T651 plate during the penetration process caused by a 20 FSP which initial velocity is 1000 m/s. In the final stage of penetration, the crack occurs which growth leads to the final separation of the plug from the plate.

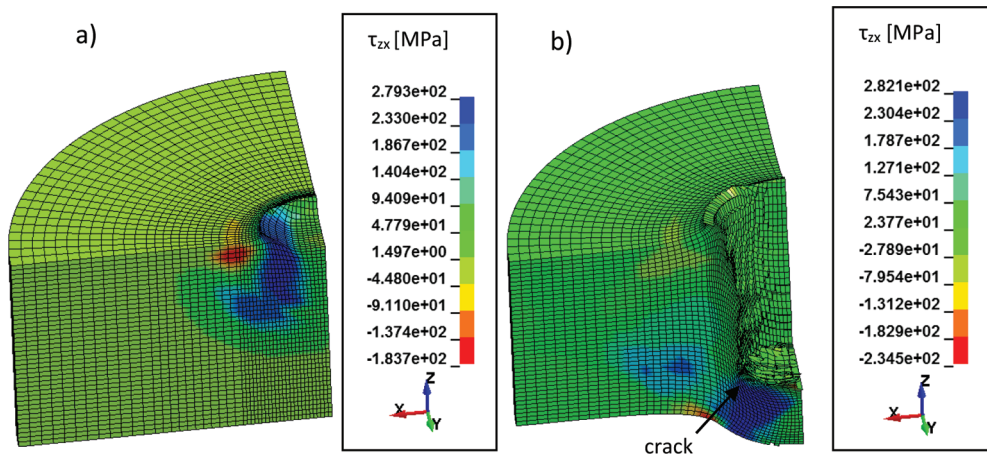


Figure 8: Maps of shear stresses at (a) the beginning of the penetration ($t = 4 \mu\text{s}$) and (b) the plug formation ($t = 80 \mu\text{s}$)

The stages of the perforation process with a decrease of the projectile velocity in time are schematically presented in Figure 9. The velocity of the projectile decreases systematically, to the moment when the projectile is fully separated from the plate and it moves with a constant velocity. The process is divided into the stages according to the model proposed by Ravid and Bodnar [32] who described the penetration of a ductile target caused by a blunt projectile. The target mass in front of the projectile is accelerated in the first stage of the dynamic plastic penetration. The formation mechanism changes into a highly localized shear zone surrounding the projectile nose leading to the bulge formation (stage II). The bulge is advancing and the damage develops in the shear zone caused by the severe plastic straining of the target elements which are close to the projectile. The bulge is highly localized, with hardly any global target deformation. When the critical damage is reached the plug is formed (stage III), the elements start to erode and the crack propagates towards the rear side of the target. In the final stage, a shear failure leads to the plug exit.

The FSP has a non-axisymmetric shape, consequently, a 3D geometry provides a proper modeling of the projectile effect on the material structure. However, considering time of calculation and the applied technique (i.e. elements erosion), the question arises if it is a unique method of the FSP impact modeling.

4.2. AXISYMMETRIC FEM AND SPH APPROACH

In numerous numerical simulations discussed in the literature, [8, 16, 21], the modeling of a material response to impacts of blunt, conical and ogive projectiles is realized by application of 2D axisymmetric models which allow for a proper estimation of a structure's behavior. In the 2D modeling, the non-axisymmetric geometry of the FSP must be approximated by the rotational quasi-conical projectile. The geometry of the axisymmetric model is given in Figure 10(a), whereas its SPH equivalent is presented in Figure 10(b).

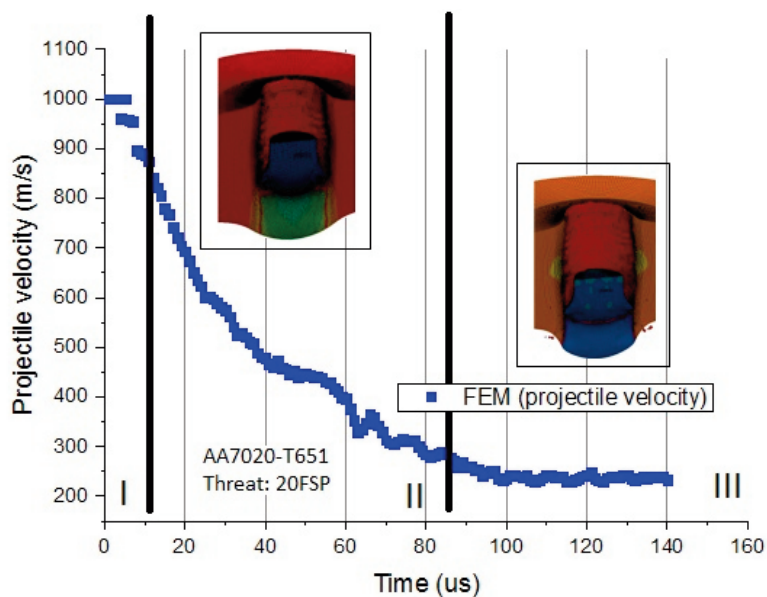


Figure 9: Schematic sequence of perforation process caused by FSP. Stage I: dynamic plastic penetration, stage II: bulge formation and advancement, stage III: beginning of crack and plug formation, stage III: plug exit

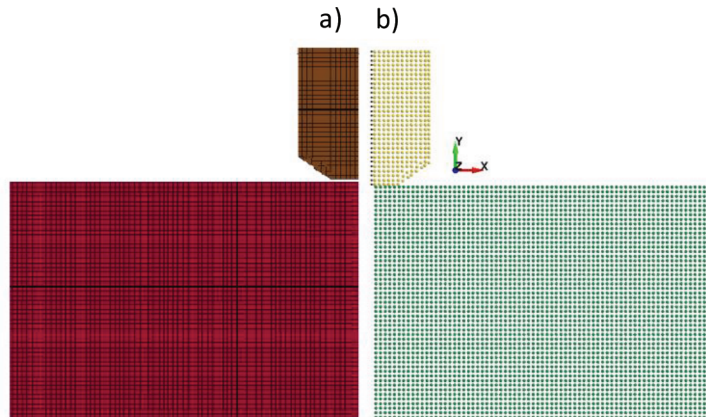


Figure 10: (a) Geometry of the axisymmetric model and (b) its SPH equivalent

The SPH geometry is built basing on the axisymmetric geometry regularly meshed, in which in the place of nodes (spacing of 0.25 mm) – SPH particles are created. In the axisymmetric plate, a number of elements is close to 3700 shell elements and 3800 nodes (placed each 0.7 mm), which are equivalent to 3800 particles in the SPH model. The axisymmetric projectile consists of 360 shell elements and 400 nodes placed regularly each 0.5 mm - which is equivalent to 400 particles in the SPH model.

In the FEM model, the contact between the projectile and plate is assumed as `*2D_AUTOMATIC_NODES TO SURFACE`, whereas in the case of the SPH model, no contact is required. No friction is assumed, either. From the calculation performed in 3D, it is concluded that the supporting plate does not affect the deformation of the impacted plate. Consequently, in the 2D tasks, the frame is not modeled and the boundary conditions are applied to the edge of the plate. The material model for AA7020-T651, i.e. the Johnson – Cook model Eqns (1–3) and the equation of state, i.e. the Grüneisen equation, Eqns (4–5), remain the same as in 3D formulation, i.e. `*MAT_015_ JOHNSON_COOK` and `*EOS_ GRUNEISEN`. The material of which projectile is made – steel 4340-H is defined by `*MAT_003_PLASTIC_KINEMATIC`, as the SPH method in Ls-DYNA does not allow the simplified version of the Johnson-Cook model to be applied. In the case of FEM modeling, the `*MAT_ADD_EROSION` is applied in which the erosion criterion is fulfilled when the shear strain at failure reaches 100%.

In Figure 11, the results of modeling in 2D axisymmetric approach are presented – the comparison between SPH and FEM is shown for the impact with an initial velocity 1000 m/s. In general, the maps of the equivalent von Mises stress show that the state of stress obtained in both models is similar, however, the detailed comparison reveals the local differences in its distribution.

Either, the resulted plug shape is different for the FEM and SPH calculations. The shape of the plug obtained in the FEM calculation is similar to that one resulted from 3D simulation, Figure 12(a)–(c). The target material is sheared on the periphery of the projectile which led to the plug separation from the plate, Figure 12(a). In the case of the SPH calculations, the shear stress on the projectile periphery is observed, Figure 12(b); however, no distinct shear bands occur. The target material is compressed under the nose of the projectile but the particles are very tightly packed – and they do not erode. Such an effect results in the increased height of the plug in comparison to the experimental one.

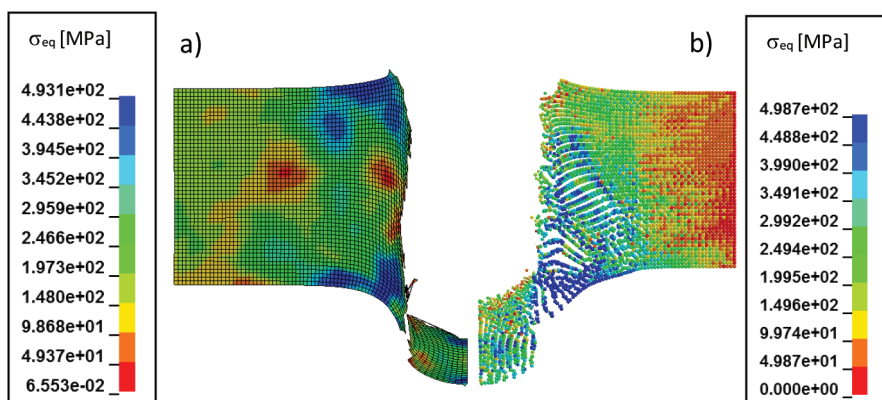


Figure 11: The maps of the equivalent Mises stress obtained due to (a) the FEM and (b) the SPH calculation at 100 μ s

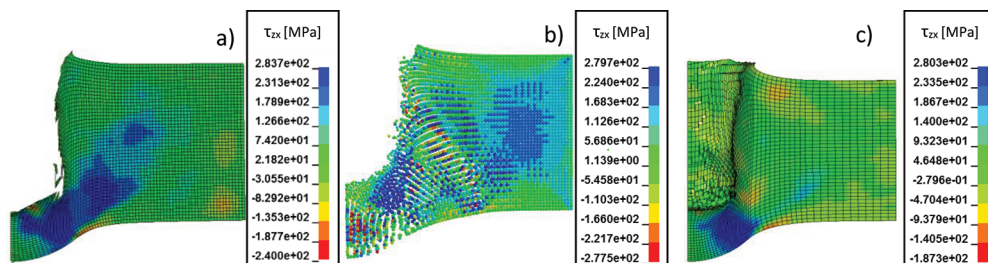


Figure 12: The maps of the shear stress resulted from the calculations obtained in (a) the axisymmetric FEM, (b) the SPH and (c) the 3D FEM at 100 μ s

The residual velocity calculated by means of two axisymmetric models is not similar. In the case of the FEM model, the impact with an initial velocity 1000 m/s results in the residual velocity close to 370 m/s - which overestimates the experimental value but it is close to the results of the 3D modeling. The SPH model gives worse results, $v_{res} = 70$ m/s. The reason of this discrepancy is an improper behavior of the target particles under the projectile's nose.

Finally, it may be concluded that the axisymmetric FEM and SPH models allow for an approximation of the FSP impact on the target material for velocities lower than 1200 m/s. The general behavior of the aluminum plate is similar in the calculations obtained by both techniques. In the case of the FEM calculation, the plug is observed but its residual velocity overestimates the expected value – which can be, however, considered as an acceptable approximation. The SPH calculations do not result in a proper modeling of the plug, the details of the obtained failure mode and accuracy of the calculated residual velocity must be improved. The SPH is a demanding technique and a simple “copying” of material models and boundary conditions from the 2D axi-symmetric model to the SPH model does not result in the same response of the material.

In the next paragraph, the authors consider the accuracy of the numerical results and ways of its quantitative evaluation. In the case of the impact modeling, the main criterion is a calculated residual velocity compared to the experimental value. If the plate perforation results in the plugging failure mode – the occurrence of a plug is also required. Consequently,

the question should be stated to what extent the geometry of a numerical plug should match the experimental plug that the simulation was considered as valid and credible. Regarding the possibilities of the modern optical scanning techniques, another criterion may be implemented to compare numerical results with experiments.

4.3. COMPARISON BETWEEN NUMERICAL RESULTS AND THE OPTICAL SCANNING OF THE PLUG

The numerical representation of the experimentally deformed target and its debris can be achieved by applications of optical methods for 3D shape reconstruction and algorithms for geometry processing. Laser and structural light scanners or photogrammetric techniques produce dense point clouds representing a scanned object. Such point clouds can be registered, connected and meshed and afterwards analyzed according to different requirements.

The scanning of the plug was performed by using the laser scanner EPPM-1, based on laser profilometer Keyence LJ-V7080 allowing for distance measurements with resolution of 5 μm [33]. The translation of the laser's head in x and y direction provides scanning of the object with steps of 0.1 mm. The complete 3D representation was obtained by fitting together several scans made in different positions of the object with subsequent changes of the angles between the object and the axis of the scanner. Each point cloud was pre-aligned and finely registered by means of the Iterative Closest Point (ICP) algorithm implemented in the program Cloud Compare [34]. The obtained point clouds provide a detailed reproduction of the plug and can be regarded as a reference geometry to be compared with numerical results. Figure 13(b) presents scanning results of the plug obtained from the impact with an initial velocity close to 950 m/s, Figure 13(a).

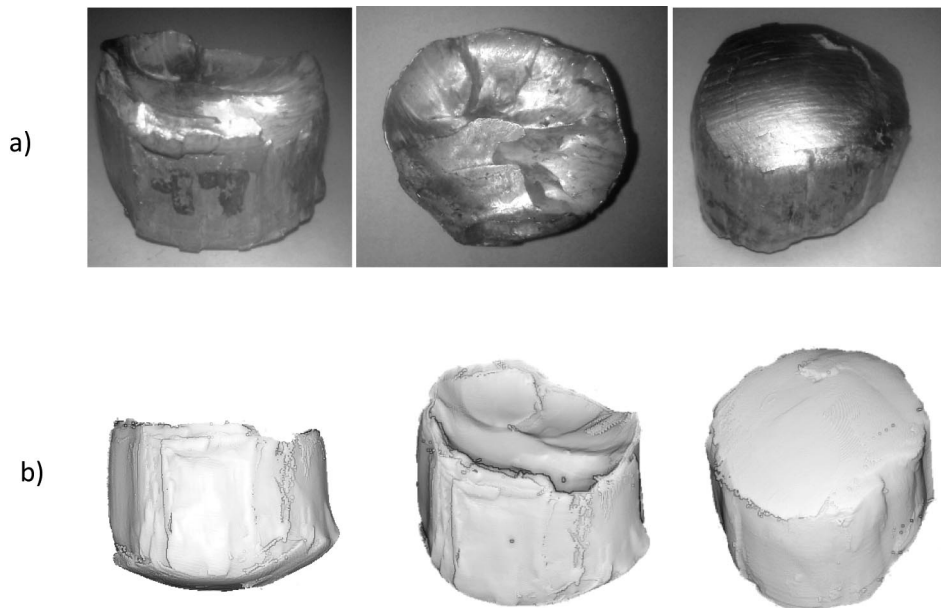


Figure 13: (a) Views of the plug resulting from the impact with an initial velocity 950 m/s and (b) point cloud representing the scanned plug

Figure 14(a) presents the geometry of a quarter of the 3D FEM numerical model. The elements of the plug (Figure 14(b)) are mirrored in order to obtain its full 3D model, Figure 14(c). Consequently, the resulted plug is symmetric.

A qualitative comparison of the geometries of plugs obtained by the 3D FEM numerical simulation and in the experiment is presented in Figure 15. Both point clouds- the numerical and scanned plug - are pre-aligned in a global coordinate system and finally positioned by means of the ICP algorithm. To obtain better visualization, the surface representing the experimental plug is colored. It is observed that both shapes are in good correspondence.

In order to provide a quantitative comparison of both point clouds, their overall dimensions are compared in Table 6. The table contains lengths of sides of bounding boxes presented in Figure 15(a–b), which are fitted in order to contain the farthest points of each point cloud. The biggest difference in the global dimensions is 1.9 mm and the mean error is

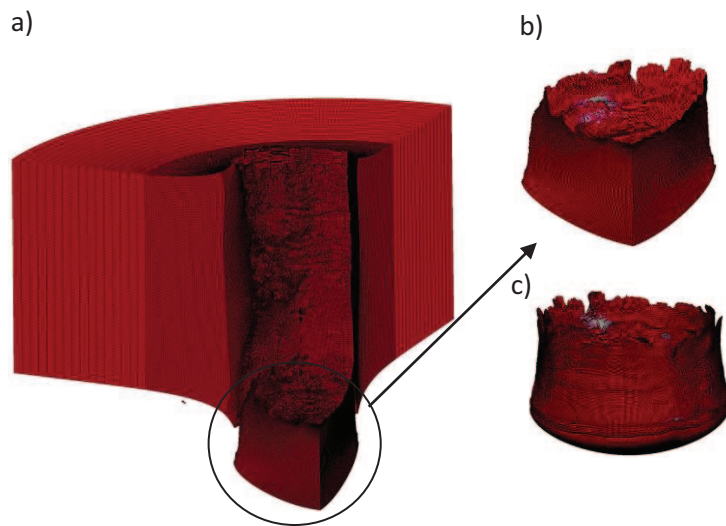


Figure 14: (a) Numerically obtained, deformed target plate, (b) 1/4 of the calculated plug and (c) the full 3D plug

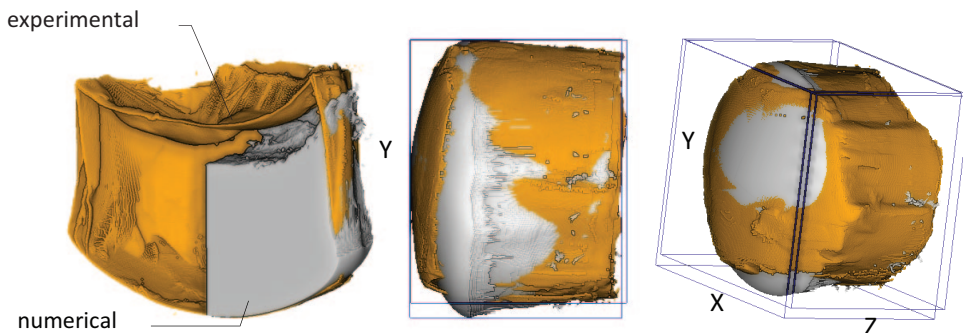



Figure 15: Comparison of shapes of plugs obtained experimentally and numerically presented also in the bounding boxes

Table 6: Dimensions of bounding boxes of compared point clouds

| Bounding box dimension | Experiment [mm] | Model [mm] | Difference [mm] |
|------------------------|-----------------|------------|-----------------|
| X | 37,5 | 36,9 | 0,6 |
| Z | 26,5 | 26,0 | 0,5 |
| Y | 32,2 | 34,1 | 1,9 |

Table 7: Dimensions of bounding boxes of compared point clouds



| Bounding box dimension | Experiment [mm] | SPH [mm] | 2D [mm] |
|------------------------|-----------------|----------|---------|
| X | 37,5 | 25,5 | 25,5 |
| Z | 26,5 | 30,5 | 15,5 |
| Y | 32,2 | 25,5 | 25,5 |

equal to 0.27 mm. Concluding, it can be stated that the overall dimensions of the numerical plug do not differ much from the dimension of the experimental plug.

Analysis of dimensions is made also for the plugs resulting from the axisymmetric FEM and SPH calculations, Table 7. In comparing to the experimental plug to the 3D plug, the dimensions of the 2D plugs do not allow for so accurate plug modeling – they are too narrow and of improper heights.

The analysis of the geometrical similarity of the plug obtained due to the simulation and experiment proves that that the techniques of optical scanning may be used as an additional criterion in evaluation of numerical calculations. Optical scanning allows for a very accurate representation of an object by point clouds which can be afterwards analyzed and compared with the deformed mesh of a numerical model. The above study is considered as a first step in the analysis of the quality of numerical results. Similar comparison of geometrical properties can be prepared for the deformed projectiles and remaining targets. This method can be regarded as an efficient technique leading to obtain a better, improved numerical simulation.

5. SUMMARY AND CONCLUSIONS

The limit curve for the AA7020-T651/FSP configuration has been determined basing on the results of the ballistic test. To understand better the phenomena which caused the material failure, the test is modeled by different numerical techniques – the 3D FEM, the axisymmetric FEM and the axisymmetric SPH. The boundary and initial conditions of the task are similar in all cases. The material model and the equation of the state applied – i.e., the Johnson Cook model Eqns (1–3) and the Gruneisen equation Eqns (4–5) - are defined by the cards *MAT_015_JOHNSON_COOK and *EOS_GRUNEISEN in the FEM and SPH calculations. The parameters of the JC model have been determined due to the own

experimental investigation. In the Lagrangian approach, the erosion criterion is applied - the elements are removed from the mesh when the shear strain reaches 100%.

As the FSP projectiles have a non-axisymmetric shape, the most accurate target – projectile behavior is achieved by the 3D FEM model. For impact velocities lower than 1200 m/s, the target failed due to the shear since it is the dominant stress state which leads to the target perforation by plugging. The calculated ballistic limit curve presents acceptable results comparing to the experimental curve, the plug shape is correct as well.

Although, the FSP shape is assumed as a quasi-conical in the axisymmetric modeling, they allow a proper approximation of the plugging failure to be calculated. Generally, both - the FEM and SPH axisymmetric models results in a correct target response to the FSP impacts with velocities lower than 1200 m/s – the shear stress on the periphery of the projectile is identified, the plug is separated and ejected from the target geometry. However, a lack of erosion in SPH calculation leads to an improper shape of the resultant plug, the residual velocity of an exemplary impact is too low, either.

The agreement between the numerical and experimental results is also checked by comparing geometrical similarity of the experimental plug and its numerical equivalent. The plug is scanned using a laser, from which the 3D shape is reconstructed in a form of a dense point cloud. The shapes of experimental plug and its numerical equivalent resulting from the 3D FEM calculation are in good agreement, though, the non-symmetrical and local features of the experimental plug are not modeled. In conclusion, the optical scanning is a promising technique helping to evaluate the results of numerical simulations.

ACKNOWLEDGEMENTS

Authors thank Mr. Christian Doenlen and Mr. Thomas Wolf for performing ballistic impact tests.

REFERNECES

- [1] Rosenberg Z and Dekel E. Terminal ballistics. 1st ed. New York: Springer, 2012.
- [2] MIL-P-46593A (Notice 1), Military Specification: Projectile, Calibers .22, .30, .50, and 20 mm Fragment-Simulating (01-JUN-1996) [S/S BY MIL-DTL-46593B].
- [3] NATO MAS. Standarization Agreement (STANAG). Procedures for evaluating the protection levels of logistic and light armoured vehicles for KE and artillery threats, 2004.
- [4] VPAM APR 2006. General basis for ballistic material, construction and product testing, 2009.
- [5] Laible R (ed.) Ballistic materials and penetration mechanics. Vol. 5. Elsevier, 2012.
- [6] Backman ME and Goldsmith W. The mechanics of penetration of projectiles into targets. *Int. J. Eng. Sci.* 1978; 16:1–99.
- [7] Børvik T, Langseth M, Hopperstad OS and Malo KA. Ballistic penetration of steel plates. *Int. J. Impact Eng.* 1999; 22. 9:855–86.
- [8] Børvik T, Langseth M, Hopperstad OS and Malo KA. Perforation of 12 mm thick steel plates by 20 mm diameter projectiles with flat, hemispherical and conical noses: part I: experimental study. *Int. J. Impact Eng.* 2002; 27. 1:19–35.
- [9] Børvik T, Langseth M, Hopperstad OS and Malo KA. Perforation of 12 mm thick steel plates by 20 mm diameter projectiles with flat, hemispherical and conical noses: part II: numerical simulations. *Int. J. Impact Eng.* 2002; 27. 1:37–64.

- [10] Kpenyigba KM, Jankowiak T, Rusinek A and Pesci R. Influence of projectile shape on dynamic behavior of steel sheet subjected to impact and perforation. *Thin Wall Struct* 2013;65:93–104.
- [11] Fras T, Colard L, Lach E, Rusinek A, Reck B. Thick AA7020-t651 plates under ballistic impact of fragment-simulating projectiles. *Int. J. Impact. Eng.* In Press, Accepted Manuscript, Available online 20 August 2015
- [12] Johnson GR and Cook WH. A constitutive model and data for metals subjected to large strains, high strain rates and high temperatures. 7th Int. Symp. on Ballistics 1983.
- [13] Johnson GR and Cook WH. Fracture characteristics of three metals subjected to various strains, strain rates, temperatures and pressures. *Eng. Fract. Mech.* 1985; 21: 1:31–48.
- [14] Zienkiewicz, Olgierd Cecil, et al. *The finite element method*. Vol. 3. London: McGraw-hill, 1977.
- [15] Zukas J. *Introduction to hydrocodes*. Elsevier, 2004.
- [16] Schwer LE and Windsor CA. Aluminum Plate Perforation: A Comparative Case Study Using Lagrange With Erosion, Multi-Material ALE, and Smooth Particle Hydrodynamics. 7th European LS-DYNA conference 2009.
- [17] Liu MB and Liu GR. Smoothed particle hydrodynamics (SPH): an overview and recent developments. *Arch. Comp. Met. Eng.* 2010;17.1:25–76.
- [18] Lucy L. A numerical approach to the fission hypothesis. *Astron J* 1977;1013–24.
- [19] Gingold RA and Monaghan JJ. Smoothed particle hydrodynamics: theory and application to non-spherical stars. *Mon. Not. Roy. Astron. Soc.* 1977;181–375.
- [20] Liu GR. *Meshfree methods: moving beyond the finite element method*. CRC press, 2009.
- [21] Swaddiwudhipong SM, Islamb J and Liu ZS. High velocity penetration/perforation using coupled smooth particle hydrodynamics-finite element method. *Int J Protective Struct* 2010; 1. 4:489–506.
- [22] Johnson GR, Stryk RA and Beissel SR. SPH for high velocity impact computations. *Comput. Method Appl. M* 1996; 139. 1:347–73.
- [23] Aktay L and Johnson AF. FEM/SPH coupling technique for high velocity impact simulations. *Advances in Meshfree Techniques* 2007; 147–67.
- [24] Zukas J. *Impact dynamics*. 1th ed. New York: John Wiley & Sons, 1982.
- [25] Woodward RL. The interrelation of failure modes observed in the penetration of metallic targets. *Int. J. Impact Eng.* 1984; 2. 2:121–9.
- [26] Gitter R. *Design of aluminium structures: selection of structural alloys*. EUROCODES-Background and Applications 2008, Brussels, Belgium.
- [27] www.aubertduval.fr/.../Plaqueette_aero_BDEF_2.pdf
- [28] Clausen AH, Børvik T, Hopperstad OS and Benallal A. Flow and fracture characteristics of aluminium alloy AA5083–H116 as function of strain rate, temperature and triaxiality. *Mat. Sci. Eng. A* 2004; 364. 1:260–72.
- [29] <http://www.dynasupport.com/news/ls-dyna-971-manual-pdf>
- [30] Steinberg DJ. *Equation of State and Strength Properties of Selected Materials*.

Lawrence Livermore National Laboratory UCRL-MA-106439 1996.

- [31] Schwer LE. A Brief Look at Mat_Non_Local: A Possible Cure for Erosion Illness? 11th International LS-DYNA Users Conference 2011.
- [32] Ravid M and Bodner SR. Dynamic perforation of viscoplastic plates by rigid projectiles. *Int. J. Engng Sci* 1983; 21:577–91.
- [33] Skłodowski M, Pawłowski P. Sprawozdanie z badań obrazu Pokłon Trzech Króli M. H. Lodera, z katedry St. Aubin de Namur w Belgii- Étap III. Projekt NCN Preludium 2, Nr UMO-2011/N/HS2/01936, 2012.
- [34] <http://www.danielgm.net/cc/>

